Investigation of short-range structural order in $Zr_{69.5}Cu_{12}Ni_{11}Al_{7.5}$, $Zr_{41.5}Ti_{41.5}Ni_{17}$ and $Zr_{67}Ni_{33}$ metallic glasses using X-ray absorption spectroscopy and *ab-initio* molecular dynamics simulations

Debdutta Lahiri [a,1], Surinder M. Sharma[a], Ashok. K. Verma[a], B. Vishwanadh[b], N. C. Das[a], G.K. Dey[b], G. Schumacher[c], T. Scherb[c], H. Riesemeier[d], U. Reinholz[d], M. Radtke[f] and S. Banerjee[e]

[a] High Pressure and Synchrotron Radiation Physics Division, Bhabha Atomic Research Centre, Mumbai 400085, India.

[b]Materials Science Division, Bhabha Atomic Research Centre, Mumbai 400085, India.

[c]Helmholtz Zentrum Berlin für Materialien and Energie, 14109 Berlin, Germany

[d] Federal Institute for Materials Research and Testing, 12205 Berlin, Germany

[e]Homi Bhabha National Institute, Mumbai 400094, India

Abstract

We have investigated the short-range-order of $Zr_{69.5}Cu_{12}Ni_{11}Al_{7.5}$, $Zr_{41.5}Ti_{41.5}Ni_{17}$ and $Zr_{67}Ni_{33}$ metallic glasses, using X-ray absorption spectroscopy and *ab-initio* molecular dynamics simulations. The glass-forming-abilities of these alloys degrade as: $Zr_{41.5}Ti_{41.5}Ni_{17} > Zr_{69.5}Cu_{12}Ni_{11}Al_{7.5} > Zr_{67}Ni_{33}$. While superior glass formation ability of the multi-component alloys is understandable from confusion principle, better glass formation ability of $Zr_{41.5}Ti_{41.5}Ni_{17}$ than $Zr_{69.5}Cu_{12}Ni_{11}Al_{7.5}$ is paradoxical from confusion viewpoint. We resolve this paradox by quantitatively assessing the relative importance of icosahedral content, configuration diversity, intra-cluster disorder and chemical interaction in these three systems. Our results establish that large difference in these parameters exists

[1]Corresponding author. Tel.: + 91 22 2559 2991; fax: + 91 22 2550 5296

Email address: dlahiri@barc.gov.in; debduttalahiri@yahoo.com (D. Lahiri)

between binary and multi-component alloys. The structure of $Zr_{67}Ni_{33}$ resembles $NiZr_2$ while that of the multi-component alloys is distributed about icosahedra. Icosahedral content and configuration distribution varies between $Zr_{41.5}Ti_{41.5}Ni_{17}$ and $Zr_{69.5}Cu_{12}Ni_{11}Al_{7.5}$. The correlation of superior glass-forming-ability of the multi-component alloys (*wrt* $Zr_{67}Ni_{33}$) with significantly increased icosahedral content is unambiguous and consistent with conventional understanding. In contrast, relative glass-forming-ability of the multi-component alloys is counter-intuitive: lower for $Zr_{69.5}Cu_{12}Ni_{11}Al_{7.5}$ (*wrt* $Zr_{41.5}Ti_{41.5}Ni_{17}$) despite ~ 11% increase in icosahedral content. We show that strong Ni-Ti chemical interaction and increased configuration diversity compete with and negate the effect of icosahedral content in $Zr_{41.5}Ti_{41.5}Ni_{17}$, thereby raising its glass-forming-ability.

1. Introduction

Glass-forming alloys have emerged over the past fifteen years with very attractive properties (e.g., high hardness, tensile strength, toughness, high elastic limit, corrosion resistance etc.) and great technological promise (e.g., spring, armor-penetrator, biomedical implants, magnetic storage material, etc.)[1-3]. Since these enhanced properties hinge on amorphous/ glassy structure, understanding the structure and its role on glass-forming-ability (GFA) of these alloys has been important for the success of metallic glasses [4-36].

Close-packed *icosahedral* units [37], incompatible with translational symmetry, have been the most widely recognized structural units of metallic glasses. Enhanced GFA is often attributed to the increased content of these units. As the number of atomic components increases, the multi-component alloy system gets confused and disfavors any preferential structural order [38]. This so-called “Confusion Principle” could result in

structural inhomogeneity (e.g. co-existing chemically ordered phases, configuration diversity), thereby promoting amorphous or glassy structure [39-42]. In general, multi-component alloys are better glass formers.

In this work, we study the short-range-order (SRO) of three alloys $Zr_{69.5}Cu_{12}Ni_{11}Al_{7.5}$ [43], $Zr_{41.5}Ti_{41.5}Ni_{17}$ [44,45] and $Zr_{67}Ni_{33}$ [46,47] having different daughter (annealed) phases and GFA. The daughter phase of $Zr_{67}Ni_{33}$ is same as $NiZr_2$ crystalline phase whereas daughter phases of $Zr_{41.5}Ti_{41.5}Ni_{17}$ and $Zr_{69.5}Cu_{12}Ni_{11}Al_{7.5}$ are quasi-crystalline (Fig. 1). GFA, inversely correlated with T_m (melting temperature) [48] on differential scanning calorimetry (DSC) curve (Fig. 2), degrades as $Zr_{41.5}Ti_{41.5}Ni_{17}$ (T_m = 800^{o}C) > $Zr_{69.5}Cu_{12}Ni_{11}Al_{7.5}$ (850^{o}C) > $Zr_{67}Ni_{33}$ (890^{o}C). While superior GFA of the multi-component alloys is understandable from the confusion perspective, better GFA of $Zr_{41.5}Ti_{41.5}Ni_{17}$ than $Zr_{69.5}Cu_{12}Ni_{11}Al_{7.5}$ is paradoxical (contradictory to confusion principle) as the latter has larger number of constituent atomic species. To resolve this paradox, we quantify the SRO of the glasses in terms of SRO type, icosahedral-SRO (ISRO) content, configuration diversity (distribution), intra-cluster disorder (distribution in bond-lengths) and chemical ordering. The relevance of these parameters *with respect to* crystallization / GFA is directly established by comparing the SRO of the glassy and annealed phases. We have derived SRO around each atom (Zr, Ni, Cu) employing X-ray Absorption Spectroscopy (XAS) and *ab-initio* molecular dynamics (AIMD) simulations [49].

X-ray absorption spectrum of any material, around the absorption edge of any of its constituent atoms, exhibits a series of oscillatory fine feature (called "structure") that modulates the monotonically decreasing atomic absorption coefficient

(μ_0), typically by a few percent. This modulation is known as "X-ray Absorption Fine Structure" (XAFS) and has been attributed to the presence of other atoms around the excited atom. The photoelectron ejected from the excited atoms gets backscattered from the neighboring atoms and interferes with the original outgoing photoelectron wave, giving rise to an oscillatory final state vector. This is the origin of the XAFS oscillations, observed in the absorption spectra. Detailed structural information about the "local" environment (up to 8-10 Å) of the excited atom, e.g., near neighbor species (*Z*), their coordination (*N*), bond-lengths (*R*) and mean square displacement (σ^2) is derived from the Fourier transformation of XAFS oscillations.

2. Experimental details

$Zr_{67}Ni_{33}$, $Zr_{41.5}Ti_{41.5}Ni_{17}$, and $Zr_{69.5}Cu_{12}Ni_{11}Al_{7.5}$ alloys were prepared from pure Zr, Ti, Al, Cu, and Ni by vacuum arc melting. To improve compositional homogeneity of the alloy, re-melting was performed six times. Prior to each re-melting, the ingot was turned upside down. The melt-spun ribbons were produced by rapidly solidifying the melted alloy, using the melt-spinning technique with a 20 cm diameter copper wheel at a surface velocity of 55 m s^{-1}. The resulting ribbons were 20-30 μm thick and ~ 5 mm wide. The composition homogeneity and amorphous character of the ribbons were confirmed by Electron Probe Micro-Analyzer (EPMA) (CAMECA, France) and X-ray diffraction (XRD) experiment, respectively (see Fig. 1).

Some of these as-cast ribbons were annealed at temperatures higher than the glass transition temperature for 1 hour (at 475°C, 537°C and 575°C for $Zr_{67}Ni_{33}$, $Zr_{41.5}Ti_{41.5}Ni_{17}$ and $Zr_{69.5}Cu_{12}Ni_{11}Al_{7.5}$, respectively) to obtain the daughter phases. The

long-range structure of the respective daughter phases was determined from XRD experiments (Fig. 1).

XAFS spectra (viz. Cu, Ni and Zr *K*-edges on as-cast and annealed ribbon samples of each alloy) were recorded in transmission mode at *BAMlin*e, BESSY [50]. Si (111) monochromator in conjunction with harmonic rejection mirror was used to filter out the required wave-lengths. Argon and Krypton filled ionization chambers were used to monitor the incident and transmitted X-ray intensities, respectively. The data were processed using ATHENA code and the resultant chi curves are shown in Fig. 3. The fast decay of XAFS oscillations beyond 10Å^{-1} is typical of amorphous materials. The data were best fitted for k^1–weighted Fourier transform (FT) over ~ 2.5-10 Å^{-1} range, using FEFF8 and FEFFIT codes [51]. Good fit quality was ensured by "*R*-factor" < 0.005 in all cases [51].

AIMD simulations were carried out for ternary and quaternary alloys using the finite temperature local density functional theory, as implemented in the Vienna *ab-initio* simulation package (VASP) [52,53]. These calculations employ projector augmented wave (PAW) potentials along with plane wave basis set. To obtain good convergence, we used the plane wave energy cut off of 450 eV. Brillouin zone integrations were carried out using Γ point. The simulations were performed on a 200 atom cubic supercell with the periodic boundary conditions. The initial configurations were prepared by randomly placing the constituent atoms inside the cubic box at densities of 6.08 and 6.76 gm cm^{-3} for ternary and quaternary systems, respectively. The simulations were carried out in a canonical ensemble (*NVT*) with a Nose´ thermostat for temperature control and the equations of motion were solved with a time step of 3 *fs*. First, the systems were melted

at 2500 K, followed by 6 ps equilibration period. Then, these systems were quenched to 300 K at the rate of ~ 12 × 10^{13} K s^{-1} (typical of *ab-initio* simulations) [52,53], followed by 6 ps equilibration period. It may be noted that the cooling rate in simulations is too fast compared to that during experimental quenching. While this may have influence on the development of medium range order, short range order is expected to be accurate [53]. The AIMD simulations for the binary system were not carried out as it adopts crystalline $NiZr_2$ phase (discussed later).

3. Results and Discussion

3.1. Structure of glassy phase

For each alloy, the Fourier transformed XAFS spectrum of glassy and daughter (annealed) phases are shown in Fig. 4. Note that the spectra in Fig. 4 are not phase-corrected. It may be noted that the peaks at less than 1.2 Å distance are not real but result from slight oscillatory character of background fit polynomial. The background oscillation arises due to limited *k*-range available (2.5-10 $Å^{-1}$). Following several background fitting strategies (e.g., different *k*-ranges, *k*-weights, *R*-ranges), the optimal background yields the observed peaks at low-*R*. It may be clarified that the low-*R* limit (~ 1.5 Å), for fitting the peak of interest (~ 1.5–3 Å), is set such that the leakage from background peak is negligible. Hence, the derived XAFS fit parameters are expected to be free of background-related artifact.

Some general features are immediately clear from Fig. 4.

1. FT amplitude for each alloy diminishes significantly beyond 3 Å, consistent with lack of long-range-order and amorphous character.
2. For each alloy, FT appears to be different at different edges, suggesting site-resolved structural inhomogeneity (consistent with earlier reports on multi-component glasses [39-42]. For example, the FT peak at Zr *K*–edge (Fig. 4(c)) is much broader than at Ni *K*-edge (Fig. 4(b)) in case of $Zr_{69.5}Cu_{12}Ni_{11}Al_{7.5}$ alloy. It is due to widely separated near neighbor distances from Zr, giving rise to one broad peak (discussed later). On the other hand, the near neighbors around Ni, Cu are located at the same radial distance (as we observe later in the analysis).
3. FT varies significantly for the different alloys systems, in terms of peak position (bond-length), peak width (disorder) etc.
4. FTs for the glassy phases appear correlated with their respective daughter phases, indicating that the crystallization process is gradual. FT-s for the annealed samples, are significantly (except $Zr_{41.5}Ti_{41.5}Ni_{17}$) sharper and their amplitudes are higher than that of the respective glasses. This indicates the improvement of local structural order upon annealing. The peak positions shift toward higher bond-lengths, corresponding to equilibrium structure.

3.1.1. $Zr_{69.5}Cu_{12}Ni_{11}Al_{7.5}$

To decipher the local structure of this alloy, we have employed both AIMD simulations and XAFS data. AIMD simulations yielded radial distribution functions, g(R) (Fig. 5(a) and (b). The nearest neighbor coordination number (N) (cut-off distance $R_{cut\text{-}off}$ = 4 Å) distribution around different sites is shown in Fig. 6(a). $R_{cut\text{-}off}$ = 4 Å has been set in the middle of the first minimum of the radial distribution function in Fig. 5. Fig. 6(a)

suggests that first shell atomic arrangement (N = 11-13) around most of the Al, Ni and Cu atoms resembles icosahedra (N=12). The distribution around Al is sharply peaked around N = 12 (ISRO) while that around most Zr atoms resembles non-icosahedral-like configuration (N = 13-15). From this distribution, the average N around each atomic species is calculated to be $N_{Al}^{AVG} = 12$, $N_{Ni}^{AVG} = 11$, $N_{Cu}^{AVG} = 10$, $N_{Zr}^{AVG} = 13$. It may be noted that N^{AVG} is dependent on the pre-defined $R_{cut\text{-}off}$ [39,54]. For example, reducing $R_{cut\text{-}off}$ to 3 Å (to match with the fit range of XAFS first peak) reduces $N_{Ni}^{AVG} = 11 \rightarrow N_{Ni}^{AVG} = 6.5$ (closer to N derived from XAFS fit, shown below).

Fig. 6(c), derived from Fig. 6(a), shows the collective coordination distribution around all the centers (*i.e*. Al, Ni, Cu, Zr centers). ISRO emerges as the SRO with highest frequency (f_{ico} = 35%) and distribution of < 13%.

Independent XAFS data fitting yielded nearest neighbor bond-lengths consistent with g(R) viz. $R_{\text{Ni-Cu/Ni}}$ = 2.6 Å, $R_{\text{Ni-Zr}}$ = 2.6 Å, $R_{\text{Cu-Cu/Ni}}$ = 2.7 Å, $R_{\text{Cu-Zr}}$ = 2.7 Å, $R_{Zr\text{-}Zr}$ = 3 Å. Note that Al parameters could not be deduced unambiguously since the stoichiometric fraction and backscattering factor of Al are much lower than those for Ni, Cu, Zr and do not affect the fit. Moreover, we could not distinguish between Ni and Cu due to similar backscattering factors (since they have similar atomic numbers). During fitting, we have used only Ni scattering to represent (Ni + Cu). Nearest neighbor coordination number around the different sites are: $N_{Ni}^{Ni+Cu+Zr} = 5$ and $N_{Zr}^{Zr} = 6$. These coordination numbers (fit results) do not increase significantly, even with the inclusion of higher cumulants during fitting [9]. In addition, the fact that these values are consistent with AIMD results for $R_{cut\text{-}off}$ = 3 Å, reiterates that the observed low coordination is real. Such reduction of nearest

neighbor coordination numbers in XAFS analysis (e.g. $N_{Ni}^{Ni+Cu+Zr} = 5$ instead of $N_{Ni}^{Ni+Cu+Zr} \sim 12$) is very typical of disordered (dislocated), multi-site configuration or nano-systems and generally these coordination numbers are termed as effective coordination number [54,55]. Thus, XAFS results indicate highly disordered SRO. The XAFS fit quality is demonstrated in Fig. 7, by comparing the data and fit spectra.

To further mutually validate XAFS and AIMD-generated atomic configurations, we have simulated XAFS spectrum around Ni using the AIMD generated atomic configuration. From the atomic coordinates in the configuration, we calculated the bond-lengths around each Ni site and the corresponding scattering paths by FEFF6. From these scattering paths, we selected the nearest neighbor paths < 4 Å. With these paths and "NOFIT" option in feffit.inp file, we generated (simulated) the site-averaged XAFS spectrum, *i.e.* by dividing the FEFFIT output by total number of Ni atoms in the cluster. The resultant XAFS simulated result (Fig. 8(a)) matches reasonably well with the experimental Ni *K*-edge XAFS spectrum. The small discrepancy between experimental and theoretical XAFS spectra may be ignored for the following reasons. The AIMD-generated atomic configuration is highly disordered and thus theoretical XAFS spectrum depends critically on the exact atomic positions. Slight relative positional displacement of atoms (for test) resulted in reduction of the amplitude by de-phasing or shift in the peak position of XAFS spectrum. By matching the theoretical and experimental spectra, we validated the AIMD-generated atomic configuration. The conclusions for Ni *K*-edge holds good for Cu *K*-edge also. Thus, both from XAFS and AIMD, the essential picture of SRO around Ni (Cu) sites is the presence of 11-13 atoms at 2.6 Å (2.7 Å) from the

center and highly disordered structure beyond that. The structure, around Zr site, could not be validated unambiguously due to larger disorder. Adding more scattering paths, around Zr site, progressively reduced the XAFS amplitude by de-phasing (Fig. 8(b)).

3.1.2. $Zr_{41.5}Ti_{41.5}Ni_{17}$

For this alloy too, we have employed both AIMD simulations and XAFS. The AIMD simulations yielded atomic configuration having radial distribution functions (g(*R*)), as shown in Fig. 5(c) and (d) and nearest neighbor coordination (N) (cut-off distance R_c = 4 Å), as shown in Fig. 6(b). Fig. 6(b) suggests site-resolved SRO viz. ISRO around the smaller atoms ($N_{Ti}^{AVG} = 12, N_{Ni}^{AVG} = 11$) and non-ISRO around Zr atom ($N_{Zr}^{AVG} = 14$). ISRO emerges as the most frequent SRO for this glass too (Fig. 6(c)). However, the proportion of ISRO is lower (f_{ico} = 24%) than in $Zr_{69.5}Cu_{12}Ni_{11}Al_{7.5}$ and the configuration has broader (ΔN = 36%) distribution.

Independent XAFS fitting yielded $R_{Ni\text{-}Ti}$ = 2.57 Å ($N_{Ni}^{Ti} = 2$), $R_{Ni\text{-}Zr}$ = 3.11 Å ($N_{Ni}^{Zr} = 1$), $R_{Zr\text{-}Ti}$= 3.06 Å ($N_{Zti}^{Ti} = 6$) and $R_{Zr\text{-}Zr}$= 3.24 Å ($N_{Zti}^{Zr} = 6$) [56,57]. These XAFS-derived nearest neighbor coordination number and bond-length results match with those of AIMD simulations. The wide separation (ΔR = 0.5 Å), between the near neighbor (Ti, Zr) distances from Ni center, represents more open and distorted structure around Ni in this alloy.

Comparing the SRO of $Zr_{41.5}Ti_{41.5}Ni_{17}$ and $Zr_{69.5}Cu_{12}Ni_{11}Al_{7.5}$, we observe that ISRO is the most populous cluster configuration for both the multi-component glasses. However, important structural differences exist within this broader framework. SRO of $Zr_{69.5}Cu_{12}Ni_{11}Al_{7.5}$ is marked by:

1. ~ 11% *increase* in f_{ico} (Fig. 6(c)), which could be due to addition of smaller atom Al.
2. ~ 23% *decrease* in the distribution of nearest neighbor configuration (Fig. 6(c)) *i.e.* improved homogeneity.
3. More efficient packing: Relatively open structure in $Zr_{41.5}Ti_{41.5}Ni_{17}$ may be attributed to the existence of strong Ni-Ti interactions. The signature of strong Ni-Ti interaction is evident from the structural parameters: (i) There is significant reduction in $R_{Ni\text{-}Ti}$ and increase in $R_{Ni\text{-}Zr,}$ from their respective sum-of-atomic-radii values; (ii) Reversed (reduced) ratio (N_{Ni}^{Zr} : N_{Ni}^{Ti}) = 0.38:1 (instead of 1.67: 1 as reported for Bergman clusters)[52] indicates several broken Ni-Zr bonds. The latter could possibly result from the weakening of Ni-Zr interaction by much stronger Ni-Ti interaction [58].

   In order to verify the existence of this chemical interaction in $Zr_{41.5}Ti_{41.5}Ni_{17}$, we calculated the orbital projected density of states (PDOS) functions for each atomic species of the two glasses. From PDOS functions (Fig. 9(a) and (b), it is obvious that the glasses are metallic as they have appreciable amount of electronic density of states at the Fermi-level. The main peaks of Cu and Ni *d* states lay few electron-volts below the Fermi-level. However, *d* states of Zr and Ti participate actively in the bonding as their main PDOS weight pass through the Fermi-level. The *p* states of Zr and Ti also contribute significantly to the bonding. The Ni *d* states lay slightly deeper in the quaternary system but they show appreciable overlap with different states of other atoms in both the systems (Fig. 9(a) and (b). From Fig. 9(b), the PDOS contribution of Ti clearly exceeds that of Zr by 50%, confirming the strong interaction of Ti - consistent with the conclusion from XAFS. This is further supported by XANES: comparison of the derivatives of the normalized spectra in Fig.

9(c) shows significantly enhanced pre-edge feature (at 8332 eV) for $Zr_{41.5}Ti_{41.5}Ni_{17.}$ The pre-edge feature results from *p-d* hybridization and is, therefore, a measure of charge transfer. The strong pre-edge feature for $Zr_{41.5}Ti_{41.5}Ni_{17}$, thus, suggests strong charge transfer to Ni - most likely from Ti. All of these unambiguously establish the existence of chemical interaction in $Zr_{41.5}Ti_{41.5}Ni_{17.}$

3.1.3. $Zr_{67}Ni_{33}$

The instability of this glass gets instantly revealed during experiments as the Ni *K*-edge spectrum evolved drastically towards more ordered structure, within the course of single scan (< 20 min). This is driven by heat infused due to large x-ray absorption at Ni *K*-edge. This rendered the Ni *K*-edge spectra of this glass unusable for analysis. Fortunately, the spectra for the annealed sample at Ni *K*-edge and for both the samples at Zr *K*-edge (due to the lower x-ray absorption at such high x-ray energy) were stable. XAFS coordination and bond-length distribution are consistent with the structure of tetragonal $NiZr_2$ (Fig. 8(c)) and are in agreement with earlier reports on Zr-rich Zr-Ni alloys [46,59-60]. Interestingly, the SRO exhibits not only nearest-neighbor correlation but conspicuous (although still small for unambiguous quantitative analysis) higher shell (second nearest neighbor around 3-4 Å) features, signifying enhanced ordering than $Zr_{69.5}Cu_{12}Ni_{11}Al_{7.5}$ and $Zr_{41.5}Ti_{41.5}Ni_{17.}$

Now comparing all the three alloys, we observe that large structural contrast distinguishes the binary ($Zr_{67}Ni_{33}$) from the multi-component ($Zr_{69.5}Cu_{12}Ni_{11}Al_{7.5}$/ $Zr_{41.5}Ti_{41.5}Ni_{17}$) glasses: SRO type ($NiZr_2$ vs. ISRO), configuration diversity (single-phase vs. heterogeneous), extent of intra-cluster order (*second-nearest*-neighbor vs. *nearest*- neighbor).

3.2. Structure of the annealed phases

SRO of the annealed phases of these alloys (Fig. 4) is found to be correlated with that of glassy phases, indicating that the crystallization process is gradual. The structural changes, upon annealing, demonstrate gradual relaxation towards respective equilibrium phase. They are marked by: (i) changes in bond-lengths by ~ 0.1 Å [e.g. in $Zr_{69.5}Cu_{12}Ni_{11}Al_{7.5}$, $R_{Ni\text{-}Zr}$ = 2.6 Å→ 2.7 Å (= $R_{Ni\text{-}Zr}$ in $NiZr_2$) upon annealing]; (ii) coordination increase (16-50%) and reduction of DWF (e.g. $\sigma^2_{Zr-Zr} = 0.022 \rightarrow 0.011\,\text{Å}^2$) representing retrieval of missing bonds and enhanced degree of order. The degree of structural evolution (defined by coordination increase), in the three alloys, follows the sequence $Zr_{41.5}Ti_{41.5}Ni_{17}$ (0%) < $Zr_{69.5}Cu_{12}Ni_{11}Al_{7.5}$ (16%) < $Zr_{67}Ni_{33}$ (50%), which is exactly opposite to their GFA (Table 1) *i.e.* GFA and structural evolution are negatively correlated (as expected).

3.3. Correlation between SRO and GFA

We have summarized the correlation between SRO and GFA for the three alloys in Table 1. We observe large difference in the SRO of binary *vs.* multi-component glasses in terms of SRO type, configuration diversity and cluster order. Further, unambiguous correlation exists between their SRO and GFA, consistent with conventional understanding.

1. Structural evolution, upon annealing, is negatively correlated with GFA.
2. SRO type ($NiZr_2$ *vs.* ISRO) - ISRO provides the basic framework of amorphous structure and *higher* ISRO content *increases* GFA of the multi-component alloys.

3. Configuration diversity (single-phase *vs.* heterogeneous) further *enhances* GFA by increasing structural confusion.
4. Extent of intra-cluster order (*second-nearest*-neighbor *vs. nearest*-neighbor) negatively correlated with GFA. Larger intra-cluster disorder in the multi-component alloys *helps* GFA by drawing more thermal energy (from annealing) to achieve ordered state. [This leaves no energy for further cluster growth and thus, restricts crystallization.]

On the other hand, SRO of the two multi-component alloys is broadly similar (ISRO, configuration diversity, large cluster disorder). Negative correlation between their ISRO content and GFA (i.e. *lower* GFA for $Zr_{69.5}Cu_{12}Ni_{11}Al_{7.5}$ despite ~ 11% *increase* in ISRO content) is counter-intuitive. To resolve this paradox, we incite the importance of strong Ni-Ti chemical interaction and increased distribution (disorder) in near neighbor configuration. Strong Ni-Ti bond arrests mobility of cluster atoms and restricts structural evolution (upon annealing) of $Zr_{41.5}Ti_{41.5}Ni_{17}$ during annealing. Both these factors compete with ISRO content and negate the latter's effect.

Thus, we observe that the role of ISRO is unambiguous for glasses with *significant* difference in ISRO content (e.g. binary vs. multi-component alloys). For glasses with comparable ISRO content (viz. $Zr_{69.5}Cu_{12}Ni_{11}Al_{7.5}$ and $Zr_{41.5}Ti_{41.5}Ni_{17}$), other parameters such as configuration disorder or chemical interaction play vital role on GFA.

4. Conclusion

With the help of XAFS measurements and AIMD simulations, we have attempted to comprehend the short-range-order of $Zr_{69.5}Cu_{12}Ni_{11}Al_{7.5}$, $Zr_{41.5}Ti_{41.5}Ni_{17}$ and $Zr_{67}Ni_{33}$

glass formers with varying glass-forming ability [$Zr_{41.5}Ti_{41.5}Ni_{17}$ > $Zr_{69.5}Cu_{12}Ni_{11}Al_{7.5}$ > $Zr_{67}Ni_{33}$]. We observe striking difference in the structure of binary *vs.* multi-component glasses in terms of icosahedral content, configuration distribution and extent of cluster order. The structure of $Zr_{67}Ni_{33}$ alloy is single-phase (resembles tetragonal $NiZr_2$) and ordered up to second nearest neighbor. On the other hand, the structure of both the multi-component alloys is site-resolved Kasper-polyhedral and distributed around icosahedral configuration. [Icosahedral content and the distribution about this configuration, of course, vary between these two alloys.] Additionally, the structure in $Zr_{41.5}Ti_{41.5}Ni_{17}$ shows signature of strong Ni-Ti interactions. We deduce that large difference in the structure of binary versus multi-component alloys ensures unambiguous and conventional correlation with their relative glass-forming-ability. In contrast, icosahedral-glass correlation is counter-intuitive between the two multi-component alloys: *lower* glass-forming-ability for $Zr_{69.5}Cu_{12}Ni_{11}Al_{7.5}$ (*wrt* $Zr_{41.5}Ti_{41.5}Ni_{17}$) despite 11% *increase* in icosahedral content. The paradox is resolved by inciting the importance of strong Ni-Ti chemical interaction and increased configuration distribution in $Zr_{41.5}Ti_{41.5}Ni_{17}$. We deduce that in alloys with broadly similar icosahedral content, such other factors become competitive and may negate the effect of the former.

Acknowledgements

DL would like to thank the Department of Science and Technology, Government of India and Helmholtz Zentrum Berlin für Materialien and Energie, Berlin, Germany for their support for the XAFS experiments.

[1] A. L. Greer, N. Mathur, Nature 437 (2005) 1246-1247.

[2] A. L. Greer, Science 267 (1995) 1947-1953.

[3] P. Ball, Nature 421 (2003) 783-784.

[4] X. D. Wang, M. Qi M, P. A.Thiel, C. Dong, Phil. Mag. 84(8) (2004) 825-834.

[5] A. Takeuchi, K. Yubuta, A. Makino, A. Inoue, J. Alloy. Compd. 483 (2009) 102-106.

[6] A. R. Yavari, Nature 439 (2006) 405-406.

[7] P. Madden, Nature 435 (2005) 35-37.

[8] I. Biazzo, F. Caltagirone, G. Parisi, F. Zamponi, Phys. Rev. Lett. 102 (2009) 195701.

[9] H. W. Sheng, Y. Q. Cheng, P. L. Lee, S. D. Shastri, E. Ma Acta Mater. 56 (2008) 6264-6272.

[10] S. Cozzini, M. Ronchetti, Phys. Rev. B 53 (1996) 12040.

[11] J. H. He, E. Ma, Phys. Rev. B 64 (2001) 144206.

[12] D. B. Miracle, Nat. Mat. 3 (2004) 697-702.

[13] H. W. Sheng, E. Ma, H. Z. Liu, J. Wen, Appl. Phys. Lett. 88 (2006) 171906.

[14] K. F. Kelton, G. W. Lee, A. K. Gangopadhyay, R. W. Hyers, T. J. Rathz, J. R. Rogers, et al. Phys. Rev. Lett. 90 (2003) 195504.

[15] D. Ma, A. D. Stoica, X. L. Wang, Z. P. Lu, M. Xu, M. Kramer, Phys. Rev. B 80 (2009) 014202.

[16] D. Ma, A. D. Stoica, L. Yiang, X. L. Wang, Z. P. Lu, J. Neuefeind, Appl. Phys. Lett. 90 (2007) 211908.

[17] N. Mattern, J. Alloy Compd. 485 (2009) 163-169.

[18] X. J. Liu, X. D. Hui, G. L. Chen, M. H. Sun, Intermetallics 16 (2008) 10-15.

[19] J. Saida, M. Matsushita, A. Inoue, Appl. Phys. Lett. 77(1) (2000) 73.

[20] W. K. Luo, H. W. Sheng, F. M. Alamgir, J. M. Bai, J. H. He, E. Ma, Phys. Rev. Lett. 92 (2004) 145502.

[21] J. Saida, T. Sanada, S. Sato, M. Imafuku, C. Li, A. Inoue, Z Kristallogr. 223 (2008) 726-730.

[22] J. Saida, T. Sanada, S. Sato, M. Imafuku, A. Inoue, Appl. Phys. Lett. 91 (2007) 111901.

[23] W. Zalewski, J. Antonowicz, R. Bacewicz, J. Latuch, J Alloy Compd. 468 (2009) 40-46.

[24] L. Yang, J. Z. Jiang, T. Liu, T. D. Hu, T. Uruga, Appl. Phys. Lett. 87 (2005) 061918.

[25] K. Saksl, H. Franz, P. Jovari, K. Klementiev, E. Welter, A. Ehnes, Appl. Phys. Lett. 83 (2003) 3924.

[26] Z. Longa, H. Wei, Y. Ding, P. Zhang, G. Xie, A. Inoue, J Alloy Compd. 475 (2009) 207-219.

[27] D. M. Herlach, Mat. Sci. Eng. R 12 (1994) 177-272.

[28] R. W. Cahn, J. Vac. Sci. Technol. A 4 (1986) 3071-3077.

[29] A. Inoue, T. Zhang, T. Masumoto, Mater. T. JIM 31 (1990) 177-183.

[30] A. Inoue, Acta Mater. 48 (2000) 279-306.

[31] Y. Q. Cheng, H. W. Sheng, E. Ma, Phys. Rev. B 78 (2008) 014207.

[32] J. Shi, M. L. Falk, Scripta Mater. 54 (2006) 381-386.

[33] H. Tanaka, J. Non-Cryst. Solids. 351 (2005) 678-690.

[34] L. Yang et al., Phys. Rev. Lett. 109 (2012) 105502.

[35] H.L. Peng, M. Z. Li, W. H. Wang, C.-Z. Wang , K. M. Ho, Appl. Phys. Lett. 96 (2010) 012901.

[36] M. Li C. Z. Wang S. G. Hao, M. J. Kramer, K. M. Ho, Phys. Rev. B 80 (2009) 184201.

[37] Note that ISRO is a geometrical conclusion that ignores real atomic sizes

[38] A. L. Greer, Nature 366 (1993) 303-304.

[39] H. W. Sheng, W. K. Luo, F. M. Alamgir, J. M. Bai, E. Ma, Nature 439 (2006) 419-425.

[40] The resolution viz. (ISRO or non-ISRO) is determined by the atomic size ratio R^* of atoms at center, shell of clusters [e.g. ISRO, for $R^* = 0.904$]

[41] Y. Q. Cheng, E. Ma, H. W. Sheng, Phys. Rev. Lett. 102 (2009) 245501.

[42] T. Fujita, K. Konno, W. Zhang, V. Kumar, M. Matsuura, A. Inoue et al., Phys. Rev. Lett. 103 (2009) 075502.

[43] U. Köster, J. Meinhardt, S. Roos, H. Liebertz, Appl. Phys. Lett. 69 (1996) 179.

[44] R. G. Henning, A. E. Carlsson, K. F. Kelton, C. F. Henley, Phys. Rev. B 71 (2005) 144103.

[45] G. W. Lee, A. K.Gangopadhyay, R. W. Hyers, T. J. Rathz, J. R. Rogers et al., Phys. Rev. B 77 (2008) 1841028.

[46] M. Matsuura, M. Sakurai, W. Zhang, A. Inoue, Mater. Sci. Forum. 539-543 (2007) 1959-1963.

[47] X. J. Liu, X. D. Hui, G. L. Chen, T. Liu, Phys. Lett. A 373 (2009) 2488-2493.

[48] Z. P. Lu, C. T. Liu, Acta Mater. 50 (2002) 3501-3512.

[49]R. Prins, D. C. Koningsberger, X-ray Absorption: Principles, Applications, Techniques of EXAFS, SEXAFS and, XANES, John Wiley & Sons, New York, 1987.

[50] http://www.bessy.de/bit/bit_show_object.html.php?i_bit_id_object=42

[51] M. Newville *et al*. Physica B 208&209 (1995) 154-156.

[52] G. Kresse, J. Hafner, J. Phys-Condens. Mat. 6 (1994) 8245-8257.

[53] G. Kresse, Furthmuller, J. Comput. Mater. Sci. 6 (1996) 15-50.

[54] H. Oji, K. Handa, J. Ide, T. Honma, S. Yamaura, A. Inoue, N. Umesaki, S. Emura, and M. Fukuhara, J. Appl. Phys. 105 (2009) 113527.

[55] H. L. Meyerheim, E. D. Crozier, R. A. Gordon, Q. F. Xiao, K. Mohseni, N. N. Negulyaev,V. S. Stepanyuk, J. Kirschner, Phys. Rev. B 85 (2012) 125405.

[56] R. G. Henning, K. F. Kelton, A. E. Carlsson and C. L. Henley, Phys. Rev. B 67 (2003) 134202.

[57] A. Sadoc, E. H. Majzoub, V. T. Huett, K. F. Kelton, J Phys-Condens. Mat. 14 (2002) 6413-6426.

[58] J. Antonowicz, A. Pietnoczka, W. Zalewski, R. Bacewicz, M. Stoica, K. Georgarakis, A.R. Yavari, J. Alloy. Compd. 509 (2011) S34-S37.

[59] X. J. Liu, X. D. Hui, G. L. Chen, T. Liu, Phys. Lett. A 373 (2009) 2488-2493.

[60] T. Fukunaga, K. Itoh, T. Otomo, K. Mori, M. Sugiyama et al., Intermetallics 14 (2006) 893-897.

***Highlights (for review)**

1. We have investigated the short-range-order of $Zr_{69.5}Cu_{12}Ni_{11}Al_{7.5}$, $Zr_{41.5}Ti_{41.5}Ni_{17}$ and $Zr_{67}Ni_{33}$ metallic glasses, using X-ray absorption spectroscopy and *ab-initio* molecular dynamics simulations.
2. With systematic and quantitative analysis, we have correlated the varying glass-formation-ability of these alloys with their different structural aspects.
3. We show that strong chemical interaction and increased configuration diversity compete with icosahedral content in modifying glass-forming-ability.

Table 1

Correlation between short-range-order and glass-forming-ability

I. $Zr_{69.5}Cu_{12}Ni_{11}Al_{7.5}$ **II. $Zr_{41.5}Ti_{41.5}Ni_{17}$** **III. $Zr_{67}Ni_{33}$**		**Correlation with GFA**
Glass-Formation-ability (GFA)	**II > I > III**	**Negative**
Degree of structural evolution, upon annealing	**II < I < III**	
f_{ico}	**III (0%) < II (24%) < I (35%)**	**Positive between III and (I, II)** **Negative between I and II**
Configuration Diversity	**II (36%) > I (13%) > II (0%)**	**Positive**
Extent of intra-cluster order	**I, II (second nearest neighbor) < III (nearest neighbor)**	**Negative**
Ni-Ti Chemical interaction	**II**	**Positive**

Figure(s)

Click here to download high resolution image

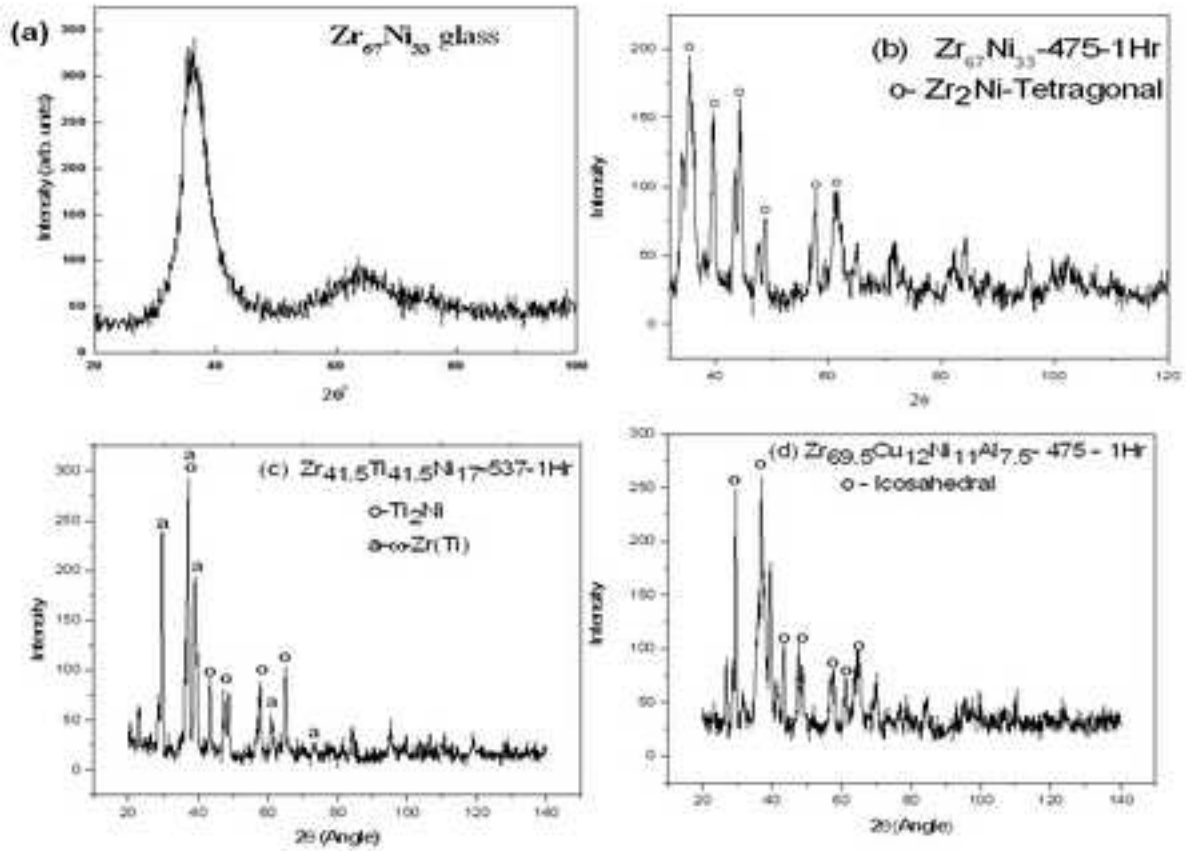

Fig. 1. XRD of (a) glassy phase of $Zr_{67}Ni_{33}$ and Annealed phases of (b) $Zr_{67}Ni_{33}$; (c) $Zr_{41.5}Ti_{41.5}Ni_{17}$; (d)$Zr_{69.5}Ni_{11}Cu_{12}Al_{7.5}$.

Figure(s)
Click here to download high resolution image

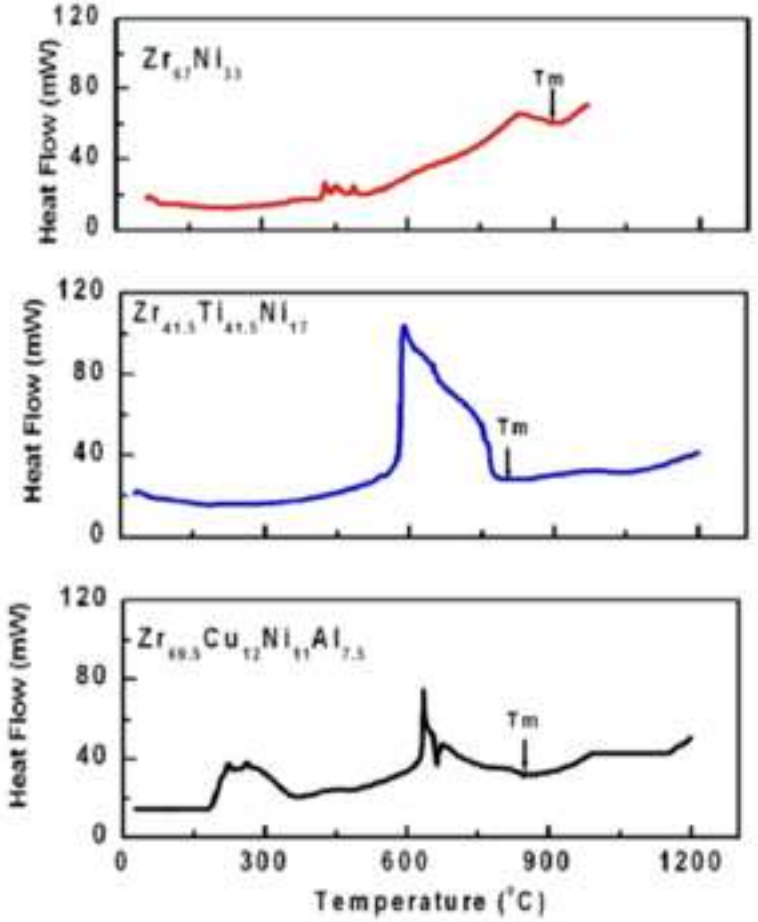

Fig. 2. DSC plots

Figure(s)

Click here to download high resolution image

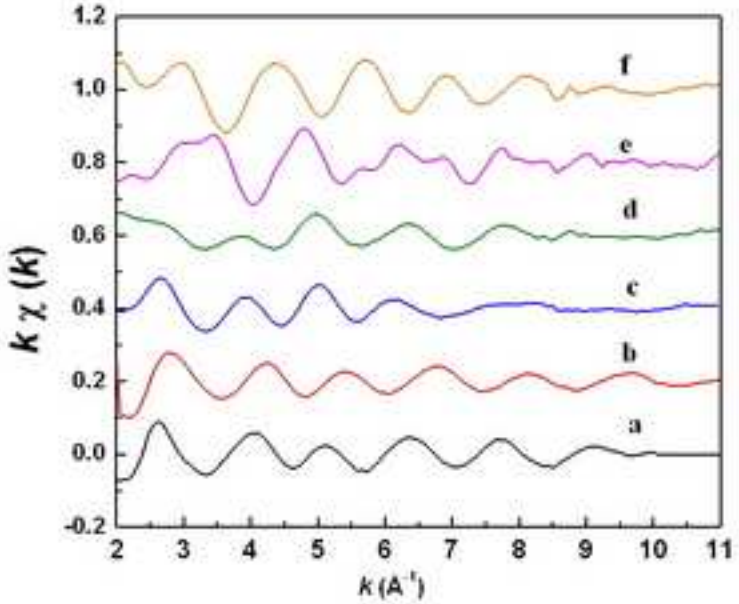

Fig. 3(a) Cu *K* (b) Ni *K* (c) Zr *K* edges of $Zr_{69.5}Cu_{12}Ni_{11}Al_{7.5}$; (d) Zr *K*-edge for $Zr_{67}Ni_{33}$; (e) Ni *K* and (f) Zr *K*-edges for $Zr_{41.5}Ti_{41.5}Ni_{17}$.

Figure(s)

Click here to download high resolution image

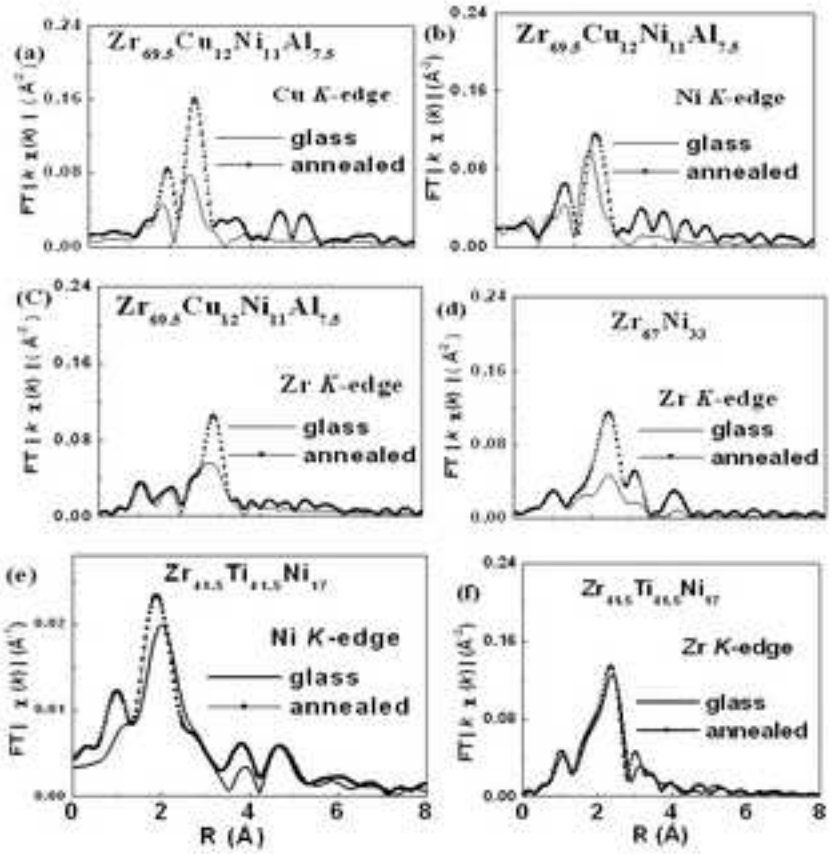

Fig. 4. XAFS data for the glasses before and after annealing

Figure(s)

Click here to download high resolution image

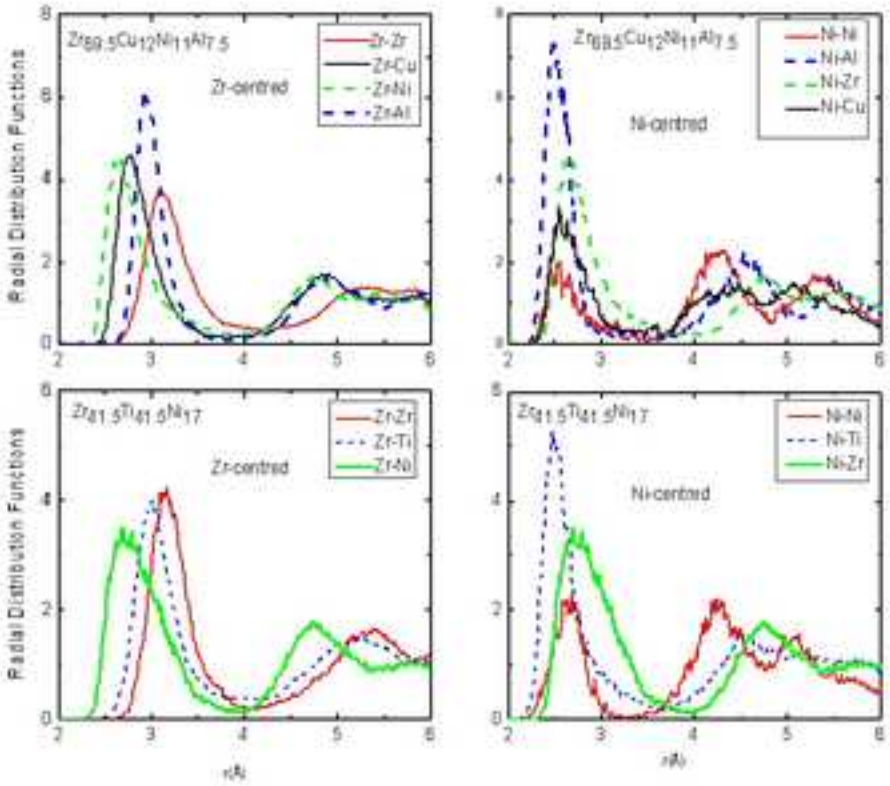

Fig. 5. AIMD simulations for $Zr_{69.5}Cu_{12}Ni_{11}Al_{7.5}$ and $Zr_{41.5}Ti_{41.5}Ni_{17}$ around Zr and Ni centers

Figure(s)
Click here to download high resolution image

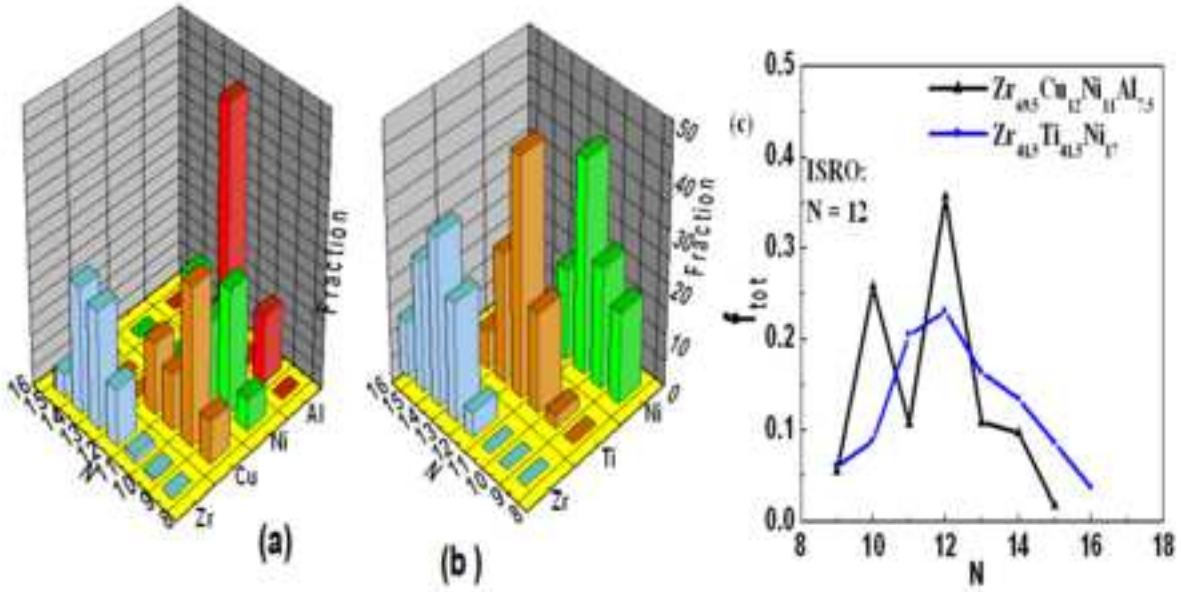

Fig. 6. Site-resolved (around each atomic species) population distribution (%) of nearest neighbor coordination for (a) $Zr_{69.5}Cu_{12}Ni_{11}Al_{7.5}$ and (b) $Zr_{41.5}Ti_{41.5}Ni_{17}$ (c) nearest neighbor coordination distribution around all the centers collectively

Figure(s)
Click here to download high resolution image

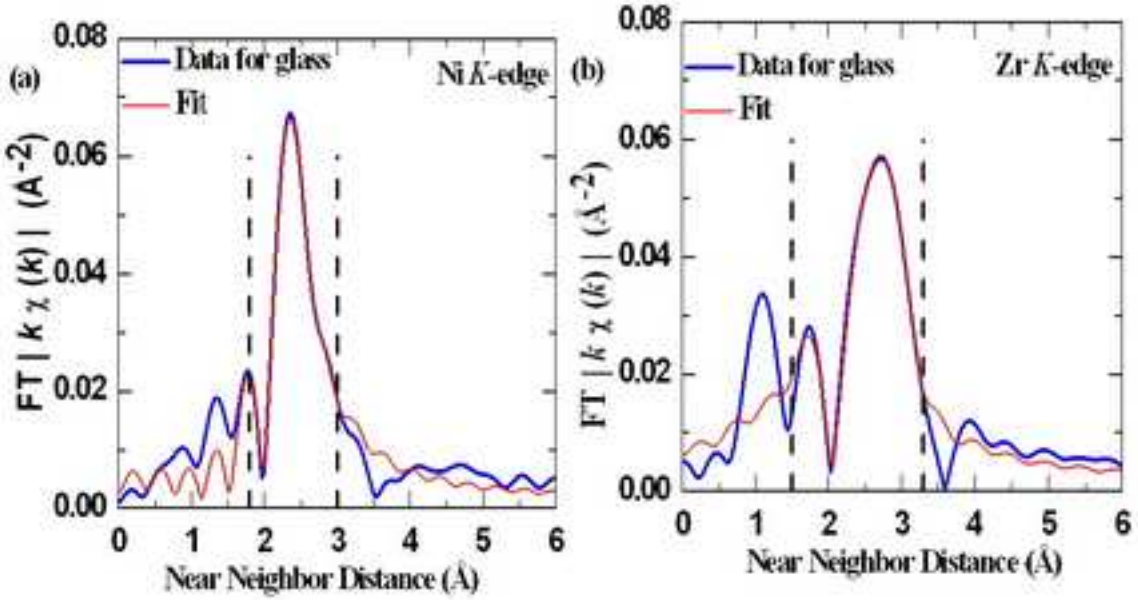

Fig. 7. Comparison of fit with data for $Zr_{69.5}Ni_{11}Cu_{12}Al_{7.5}$ glass

Figure(s)

Click here to download high resolution image

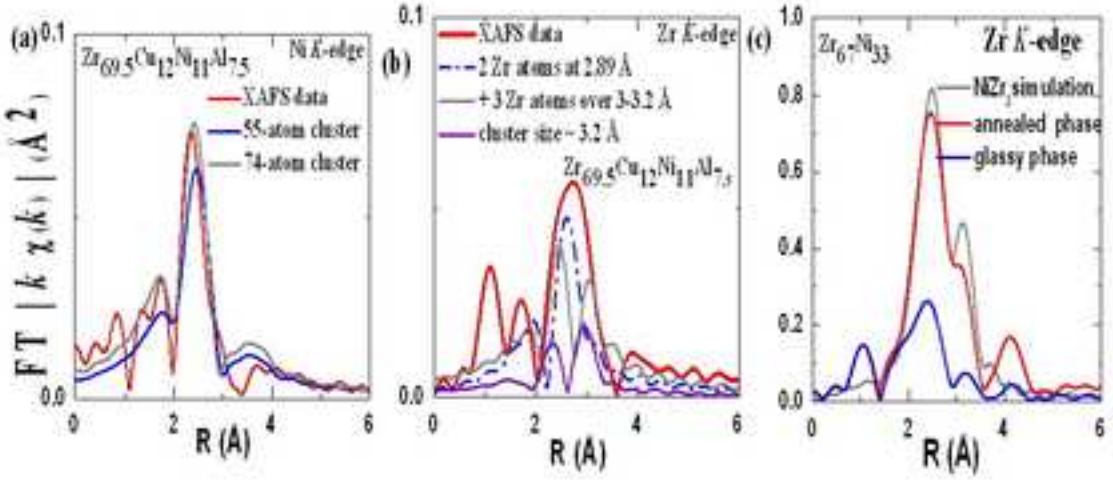

Fig. 8. XAFS data compared with FEFF simulations generated from AIMD cluster configuration for $Zr_{69.5}Cu_{12}Ni_{11}Al_{7.5}$ around (a) Ni and (b) Zr; (c) Zr *K*-edge XAFS data for $Zr_{67}Ni_{33}$ compared with FEFF simulations constructed from $NiZr_2$ structure.

Figure(s)
Click here to download high resolution image

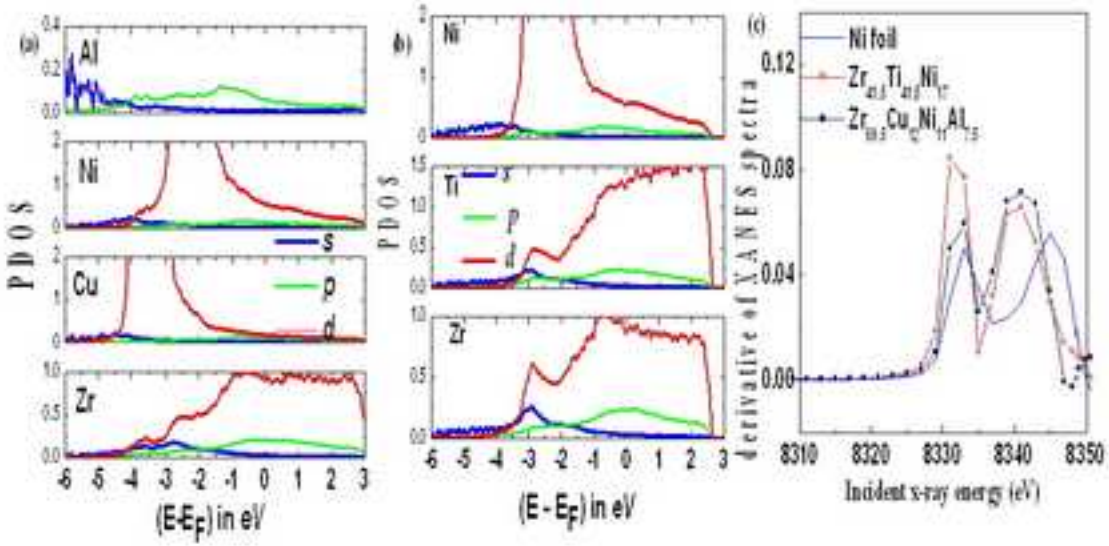

Fig. 9. Atom projected electronic density of states PDOS (states eV^{-1}atom^{-1}) of (a) $Zr_{60.5}Cu_{12}Ni_{11}Al_{7.5}$ and (b) $Zr_{41.5}Ti_{41.5}Ni_{17}$ glasses; (c) derivate of XANES spectra for these glasses compared with Ni foil.